

Pulse electrodeposited bismuth-tellurium superlattices with controllable bismuth content

Aliaksei Bakavets^{1,2}, Yauhen Aniskevich^{1,2}, Oleg Yakimenko², Jae Hyeon Jo³, Edita Vernickaite⁴, Natalia Tsyntsaru⁴, Henrikas Cesiulis⁴, Liang-Yin Kuo^{5,6}, Payam Kaghazchi⁶, Genady Ragoisha¹, Seung-Taek Myung^{3*}, Eugene Streltsov²

¹*Research Institute for Physical Chemical Problems, Belarusian State University, Minsk, 220006, Belarus*

²*Chemistry Department, Belarusian State University, Minsk, 220030, Belarus*

³*Department of Nano Technology and Advanced Materials Engineering, Sejong University, Gunja-dong, Gwangjin-gu, Seoul 05006, South Korea*

⁴*Department of Physical Chemistry, Faculty of Chemistry, Vilnius University, Vilnius, Lithuania*

⁵*Physikalische und Theoretische Chemie, Institut für Chemie und Biochemie, Freie Universität Berlin, Takustraße 3, 14195 Berlin, Germany*

⁶*Forschungszentrum Jülich GmbH, Institute of Energy and Climate Research (IEK-1), Materials Synthesis and Processing, Wilhelm-Johnen-Straße, 52425 Jülich, Germany*

**e-mail: smyung@sejong.ac.kr*

Abstract

Keywords: Bismuth telluride; bismuth; superlattice; thermoelectric materials; electrodeposition

Superlattice structures of $(\text{Bi}_2)_m(\text{Bi}_2\text{Te}_3)_n$ series with controllable Bi mole fraction from 0.41 to 0.71 are electrodeposited in pulse potentiostatic mode from acidic electrolytes containing $\text{Bi}(\text{NO}_3)_3$ and TeO_2 as precursors. Two valence states of bismuth in superlattices are identified by X-ray photoelectron spectroscopy (XPS). One of those states is attributed to interlayered Bi^0 which is present in $(\text{Bi}_2)_m(\text{Bi}_2\text{Te}_3)_n$ superlattice in the form of biatomic layers between bismuth telluride quintuples. X-ray diffraction (XRD) analysis and density functional theory (DFT) calculations indicate an increase in subcell

parameter a_{sub} and decrease in subcell parameter c_{sub} with the increase of Bi mole fraction. Biatomic layers of Bi^0 are identified with cyclic voltammetry by characteristic anodic peak between potentials of metallic bismuth and Bi_2Te_3 oxidation. The selective oxidation of Bi-bilayers in $(\text{Bi}_2)_m(\text{Bi}_2\text{Te}_3)_n$ superlattice at the potential of the anodic peak results in the product corresponding to Bi_2Te_3 by stoichiometry, but having an expanded crystal structure. Superlattices with controllable Bi mole fraction and Bi_2Te_3 with "memory effect" may be of interest for design of new thermoelectric materials with controllable parameters.

1. Introduction

Synthesis of superlattice structures of the infinitely adaptive series $(\text{Bi}_2)_m(\text{Bi}_2\text{Te}_3)_n$ with variable bismuth content is of special interest due to the emerging opportunity of controllable amount of metal introduction at van der Waals planes between Te-Bi-Te-Bi-Te quintuples in the layered structure of bismuth telluride[1] and thus controlling anisotropic electron and heat transport, which is essential in thermoelectric material and topological insulator design[2–5]. Bi^0 is present in $(\text{Bi}_2)_m(\text{Bi}_2\text{Te}_3)_n$ superlattice in the form of biatomic layers between bismuth telluride quintuples, so the variability of bismuth content is provided by variable distribution of bismuth biatomic layers in the parent Bi_2Te_3 layered structure. Previously, $(\text{Bi}_2)_m(\text{Bi}_2\text{Te}_3)_n$ superlattices were obtained by synthesis in the solid state[1,6,7] and sputtering[8].

On the contrary to high temperature solid-state synthesis which controls the target composition by temperature, the electrochemical synthesis controls the composition by electrode potential. The electrode potential drives the solid-state synthesis at mild conditions in aqueous medium, which allows preparation of various, even metastable, structures. Electrochemical equipment is simpler and more common than vacuum deposition techniques, which makes electrochemical deposition cheap and easy-scalable for practical application[9,10]. Pulse periodic potential control was used in this work to maintain uniform mass transport conditions over the whole deposition period and to control metallic bismuth oxidation, while preventing bilayers (Bi_2) anodic oxidation. Additionally, pulse deposition favors high substrate-film adhesion and proper film solidity[11–16].

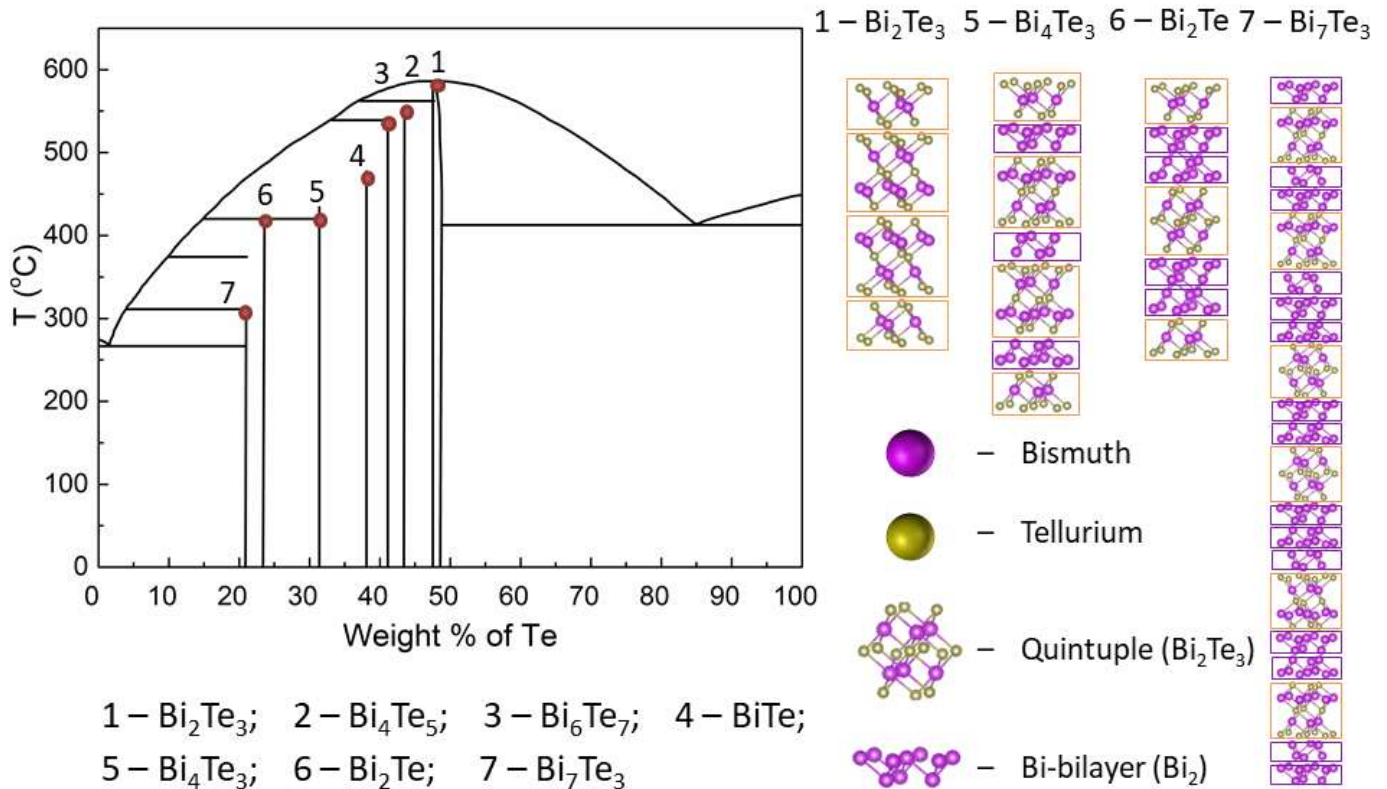


Figure 1. Bi–Te binary phase diagram with unit cells of some stoichiometric compounds. Bi_2Te_3 quintuples are outlined by orange and Bi-bilayers by purple rectangles.

Bi–Te binary phase diagram[17] (Figure 1) predicts the formation of a series of stoichiometric compounds. Any composition between vertical lines corresponding to Bi_2Te_3 and Bi_7Te_3 is possible, according to Anderson[18], and represents a superlattice of $(\text{Bi}_2)_m(\text{Bi}_2\text{Te}_3)_n$ which lacks translational symmetry in the direction of Bi_2Te_3 quintuple and Bi-bilayer stacking at high bismuth content (Figure 1). For this reason, special method of XRD to proof the variable superstructure based on analysis of subcell parameters of the supelattice was applied in this work, following the approach used earlier in[1,6,19]. Cyclic voltammetry was used to distinguish the interlayer Bi^0 from metallic Bi^0 by their potentials of anodic oxidation and to set parameters of pulse electrodeposition. Bismuth in different oxidation states in the superlattices was distinguished by X-ray photoelectron spectroscopy. Elemental composition was derived with atomic absorption spectroscopy analysis, energy-dispersive X-ray analysis and mapping of elements in high-resolution transmission electron microscopy. The High resolution transmission electron microscopy (HRTEM) provided direct observation of change in parameter a with increase of bismuth

mole fraction which was consistent with XRD data.

2. Experimental

Stainless steel substrates were pretreated in the concentrated nitric acid, polished with 0.05 μm alumina suspension and subjected to ten potential cycles between -0.4 V and 0.8 V at 50 mV s^{-1} in 3 $\text{mol}\cdot\text{L}^{-1}$ nitric acid. $\text{Bi}(\text{NO}_3)_3$ and TeO_2 were used as precursors in the subsequent electrodeposition of Bi_2Te_3 and $(\text{Bi}_2)_m(\text{Bi}_2\text{Te}_3)_n$. Molar concentration ratio ($c(\text{Bi}^{3+})/c(\text{TeO}_2)$) was varied as $2/3$, $1.1/1$, $2.7/1$, $5/1$, and $10/1$, while the sum of the concentrations was kept constant ($c(\text{Bi}^{3+}) + c(\text{TeO}_2) = 30$ $\text{mmol}\cdot\text{L}^{-1}$ in strongly acidic 3 $\text{mol}\cdot\text{L}^{-1}$ HNO_3).

Electrodeposition was carried out in the periodic pulse potential control mode in a three-electrode cell with working electrode, $\text{Ag}|\text{AgCl}|\text{KCl}(\text{sat})$ reference, and Pt counter electrode. Gamry Series G300 potentiostat was used for pulse potentiostatic deposition and cyclic voltammetry (CV). The cathodic deposition at -0.1 V was followed by the ten times longer anodic phase at the potentials derived from CV for electrolytes with various concentrations. The anodic potential was set in the range of metallic bismuth anodic oxidation which prevented the superlattice growth from disturbance by 3D bismuth particles nucleation. Pulse frequency was 1 Hz. The films were deposited for 120 minutes with stirring of the electrolyte solution, rinsed with distilled water and afterwards annealed at 250 $^\circ\text{C}$ in nitrogen for 2 hours.

XRD patterns were recorded with Empyrean X-ray diffractometer (PANalytical, Netherlands) ($\text{CuK}\alpha$ radiation with $\lambda = 1.5406$ \AA). Profile fitting of the XRD patterns was carried out using Jana2006 program[20].

The electrodeposited films were studied by scanning electron microscopy (LEO 1420) and transmission electron microscopy (JEM-3010, JEOL). Energy-dispersive X-ray spectroscopy (EDX) composition of the films was determined using Hitachi TM3000 (15 kV).

XPS analysis of samples was performed with ESCALAB MKII (VG Scientific) spectrophotometer. XPS data were analyzed using XPSPeak41 program. NIST XPS database[21] was used for reference data.

Atomic absorption spectroscopy was performed with PerkinElmer AAnalyst 400 spectrometer. Both bismuth and tellurium were analyzed in the solution obtained by dissolution of Bi_xTe_y films in nitric acid and dilution to the concentration of the calibration curve. Calibration curves for bismuth and tellurium were recorded for individual solutions of Bi(III) and Te(IV) which were prepared by dissolution of elemental Bi and Te in concentrated nitric acid followed by dilution. Bismuth was quantitatively analyzed at wavelength 214.28 nm (calibration concentration range 5 ppm – 35 ppm). Tellurium was quantitatively analyzed at wavelength 223.06 nm (calibration concentration range 5 ppm – 35 ppm).

Density functional theory calculations were carried out using the projector-augmented plane-wave (PAW) method implemented in the Vienna Ab Initio Simulation Package (VASP)[22].

The generalized gradient approximation (GGA) exchange-correlation functional proposed by Perdew, Burke, and Ernzerhof (PBE)[23] together with the D3 dispersion correction proposed by Grimme [24] was applied. To model bulk tellurides we used $1\times 1\times 1$ unit cells, a Monkhorst-Pack k-point mesh of $6\times 6\times 1$, $6\times 6\times 1$, and $6\times 6\times 2$ for 17-1 (Bi_2Te_3), 52 (Bi_4Te_3), and 72 (Bi_2Te) and an energy cut off of 400 eV.

3. Results and discussion

3.1. Cyclic voltammetry

Figure 2 *a* shows cyclic voltammograms of stainless steel electrode in the acidic solutions of individual $\text{Bi}(\text{NO}_3)_3$, TeO_2 and in the mixed Bi(III) and Te(IV) solutions at high $c(\text{Bi}^{3+})/c(\text{TeO}_2)$ ratio. Metallic bismuth electrodeposition (black curve) starts at -0.08 V and shows a typical autocatalytic/nucleation loop after scan reversal with the cathodic current of bismuth deposition up to the reversible redox potential of $\text{Bi}^{3+}/\text{Bi}^0_{(\text{bulk})}$ at 0.0 V, followed by a sharp peak of metallic bismuth anodic oxidation (peak **A**) and no further significant current above 0.1 V. Tellurium cathodic deposition (blue curve) starts in the region of bismuth cathodic deposition and shows a sluggish cathodic current continuing through the region of bismuth anodic peak in the reverse scan. The electrochemically irreversible cathodic deposition turns into the anodic oxidation close to 0.5 V with the peak current at approx. 0.6 V (peak **D**).

In the electrolyte that contains both Bi^{3+} and TeO_2 at high $c(\text{Bi}^{3+})/c(\text{TeO}_2)$ ratio, the cathodic current starts to rise at potentials below the reversible redox potential of $\text{Bi}^{3+}/\text{Bi}^0_{(\text{bulk})}$ and shows a loop in the reverse scan in the range of bismuth anodic oxidation. Interestingly, two anodic peaks (**B** and **C**) were observed in the anodic scan at high $c(\text{Bi}^{3+})/c(\text{TeO}_2)$ ratio. The peak **C** which is somewhat below the anodic oxidation peak of elemental Te is a known peak of Bi_2Te_3 anodic oxidation[25–28]. In contrast, the nature of peak **B** had no consistent explanation in literature for Bi_2Te_3 cathodic deposition: Ma et al.[25] assumed formation of some Bi-rich phases whereas Martín-González et al.[28] related this peak to the oxidation of bismuth on the Bi_2Te_3 surface.

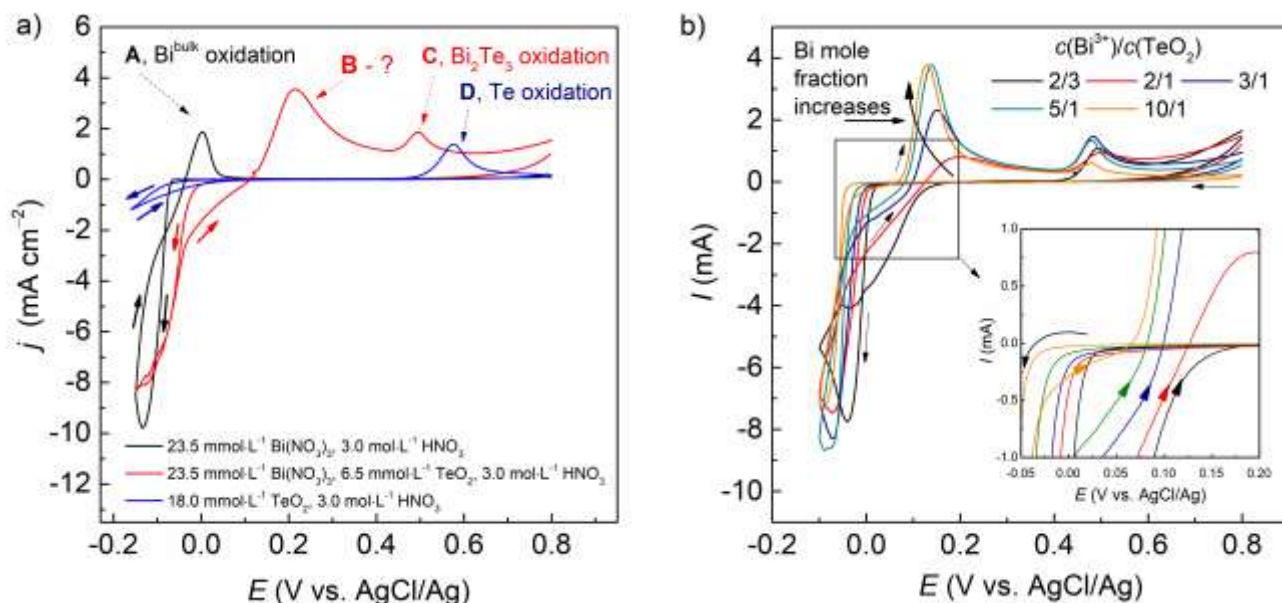


Figure 2. Cyclic voltammograms ($dE/dt = 20 \text{ mVs}^{-1}$) of stainless steel electrode at variable composition of electrolyte: (a) Bi₂Te₃ deposition bath and individual solutions of its components, (b) Bi₂Te₃ deposition electrolytes with variable Bi³⁺/TeO₂ ratio.

The occurrence and potential of peak **B** depends on the $c(\text{Bi}^{3+})/c(\text{TeO}_2)$ ratio in the electrolyte (Figure 2 b). The peak **B** was absent at $c(\text{Bi}^{3+})/c(\text{TeO}_2)$ ratio close to or lower than its stoichiometric value (2/3) in bismuth telluride, and only peak **C** was characteristic to a deposit at low $c(\text{Bi}^{3+})/c(\text{TeO}_2)$. The peak **B** emerges above $c(\text{Bi}^{3+})/c(\text{TeO}_2) = 2/3$, grows with $c(\text{Bi}^{3+})/c(\text{TeO}_2)$ up to 3/1, shows no further dependence on $c(\text{Bi}^{3+})/c(\text{TeO}_2)$ up to 10/1. On the contrary, the anodic peak **C** (Bi₂Te₃ anodic oxidation) shows no significant dependence on $c(\text{Bi}^{3+})/c(\text{TeO}_2)$, except a decrease at very high (10/1) $c(\text{Bi}^{3+})/c(\text{TeO}_2)$ ratio. The potential of peak **B** and the potential of the transition from cathodic deposition to anodic oxidation (Figure 2 b, insert), shift negatively with Bi³⁺ content in the electrolyte solution, i.e. in the opposite direction to the Nernstian shift of the reversible redox potential of Bi³⁺/Bi⁰_(bulk) redox system. Also, the potential of peak **B** is significantly higher than that for bulk metallic bismuth anodic oxidation (peak **A**), thus peak **B** was unlikely to be attributed to metallic bismuth. Also, charges corresponding to peak **B** were too high for surface limited reactions; neither anodic oxidation of surface layer of Bi atoms of Bi₂Te₃[28], nor anodic oxidation of Bi adatoms on Bi₂Te₃ which we described earlier[29,30], could explain the magnitude and behavior of this peak; on the contrary, the behavior of peak **B** was consistent with our expectation of Bi₂Te₃ contamination by (Bi₂)_m(Bi₂Te₃)_n at high $c(\text{Bi}^{3+})/c(\text{TeO}_2)$ in Bi₂Te₃

deposition bath, with attribution of peak **B** to anodic oxidation of bismuth biatomic layers. In order to obtain films of individual $(\text{Bi}_2)_m(\text{Bi}_2\text{Te}_3)_n$, the conditions of the cathodic deposition were tuned in favor of its formation by using periodic pulse potential mode with separately controlled potentials of the cathodic and anodic reactions. The anodic potential was set in the region of metallic bismuth oxidation, though keeping it low enough to prevent anodic oxidation of bilayers (Bi_2). The formation of the bilayers and their stability at the potential of metallic bismuth anodic oxidation may be related to Bi adatoms which are formed on bismuth telluride surface in underpotential range[29]. The cathodic deposition of bismuth atomic monolayer on bismuth telluride is more favorable thermodynamically than the cathodic deposition of metallic bismuth (the deposition of adlayer proceeds at more positive electrode potential [29]). Bismuth bilayer which is formed at van der Waals plane between bismuth telluride quintuple is a product of joining two bismuth atomic layers. Both atomic layers in the bilayer are stabilized by interaction with bismuth telluride, so the redox potential of Bi bilayer also appears in the underpotential region, which provides a route for the superlattice formation omitting formation of bismuth metallic phase. Besides favoring the bismuth bilayer electrodeposition and preventing the nucleation of metallic Bi, the periodic switching between the cathodic and anodic potentials under the pulse deposition mode helped to avoid depletion of precursors in the electrochemical reaction area. Thus, controlled uniform electrodeposition resulted in the formation of compact films with good adhesion to the substrate.

3.2. Pulse potential electrodeposition

The $(\text{Bi}_2)_m(\text{Bi}_2\text{Te}_3)_n$ films were electrodeposited onto steel under control of the deposition and refinement at intermittent potentials of Bi_2Te_3 cathodic deposition and bismuth anodic oxidation. Pulse frequency was set to 1 Hz with the deposition potential (E_{dep}) at -0.10 V and 10% duty cycle. The potential of the anodic phase was set from CV data for each $c(\text{Bi}^{3+})/c(\text{TeO}_2)$ as the potential of the end of the cathodic current loop before the peak **B** (insert in Figure 2 *b*). The purpose of applying the anodic stage at $c(\text{Bi}^{3+})/c(\text{TeO}_2)$ dependent potentials was to oxidize anodically nuclei of bulk bismuth phase with preservation of bismuth bilayers which were presumably associated with the anodic peak **B**.

Figure 3 *a* shows a voltammetric profile of the cathodic and anodic currents in the electrolyte used for the superlattice electrodeposition and also time profiles (inset) of the potential $E(t)$ and current $I(t)$ in the pulse electrodeposition of the superlattice. The potentials of the cathodic deposition and anodic refinement of the pulse electrodeposition are indicated by arrows at the voltammetric profile. The elemental composition of the films obtained at 30 min under periodic pulse deposition is given in Figure 3 *b* as a function of electrolyte composition. The films composition was analyzed using atomic absorption spectroscopy with independent determination of Bi and Te. The sum of Bi and Te constituents matched well the mass of the films. The negative pulses of potential (inset in Figure 3 *a*) generate pulses of cathodic current related to the electrodeposition whereas sharp peaks of positive current with small area under $I(t)$ curves are likely to result mostly from capacitive current with minor contribution of the anodic current related to the oxidative refinement of the growing film.

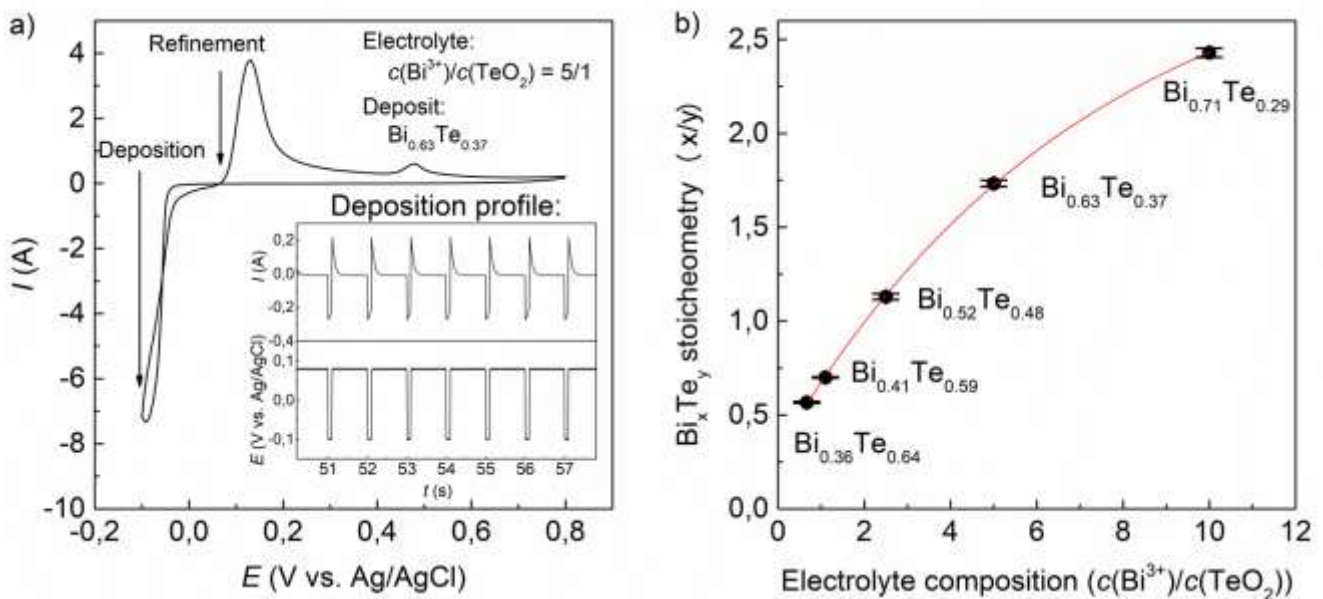


Figure 3. (a) Cyclic voltammetry of stainless steel electrode. The insert shows the controlled electrode potential profile and a current response profile during the pulsed electrodeposition of $(\text{Bi}_2)_m(\text{Bi}_2\text{Te}_3)_n$ films. (b) Dependence of the stoichiometry of Bi_xTe_y electrodeposit on relative concentrations of the both precursors in the electrolyte.

The elemental composition of deposit is a function of $c(\text{Bi}^{3+})/c(\text{TeO}_2)$ ratio in the electrolyte solution. An almost linear region of the dependence is observed for the low ratios whereas the slope of the graph

decreases at high $c(\text{Bi}^{3+})/c(\text{TeO}_2)$ ratio. Thus, the atomic Bi/Te ratio in the product of the bipotential controlled periodic pulse deposition can be efficiently managed by the electrolyte composition.

3.3. XRD analysis

Figure 4 *a-d* shows XRD patterns of Bi_xTe_y films deposited from electrolytes with different $c(\text{Bi}^{3+})/c(\text{TeO}_2)$ ratio and annealed under N_2 atmosphere at 250 °C for 2 hours. We found that annealing did not influence on the phase composition and only improved the degree of crystallinity which allowed applying more accurately the subsequent profile fitting in the XRD patterns. The profile fitting was carried out using Jana2006 program[20]. Basis subcell of $R\text{-}3m$ symmetry with approximate lattice parameters $a_{sub} = 4.4 \text{ \AA}$, and $c_{sub} = 6.0 \text{ \AA}$ was used for the refinement. Modulation vector was not included in the refinement procedure, as insufficient number of satellites was registered using $\text{CuK}\alpha$ radiation to provide convergence of γ value.

The refined subcell parameters are in good agreement with the data obtained by Bos et al.[1] for $(\text{Bi}_2)_m(\text{Bi}_2\text{Te}_3)_n$ superlattices. Furthermore, we applied the stacking model proposed in[1] to calculate lattice parameters for ideal (i.e. neglecting interlayer interactions) stacks of Bi_2Te_3 quintuples and Bi-bilayers. Also, we derived a_{sub} and c_{sub} parameters from Bi_2Te_3 , Bi_4Te , and Bi_2Te structures optimized through a DFT calculation. DFT calculations take account of electron-electron interactions between atoms in a unit cell which assumes the account of interlayer interactions. The subcell parameters a_{sub} and c_{sub} derived from XRD and the parameters calculated from the stacking model and DFT are presented in Figure 4 *e,f*. Similarly to the data of Bos, our c_{sub} parameter is somewhat smaller than the one derived from the stacking model and decreases with bismuth content. DFT calculations agree with the decrease of c_{sub} parameter when interlayer interactions are considered. XRD, DFT, and stacking model give almost identical a_{sub} parameters at low bismuth content, with some divergence emerging with bismuth content increase. The a_{sub} increases slightly slower with bismuth content than the same parameter obtained from stacking model and DFT, differently to the case of a_{sub} of $(\text{Bi}_2)_m(\text{Bi}_2\text{Te}_3)_n$ superlattices obtained by high-temperature route, which exceeded the a_{sub} of the stacking model. The slower increase of a_{sub} with

bismuth content in the electrodeposits may be ascribed to a less equilibrium state of these superlattices compared to the product of high temperature synthesis. Nevertheless, the increase of a_{sub} and decrease of c_{sub} parameters with bismuth content are in good agreement with the model which implies Bi-bilayers inclusion between Bi_2Te_3 quintuples.

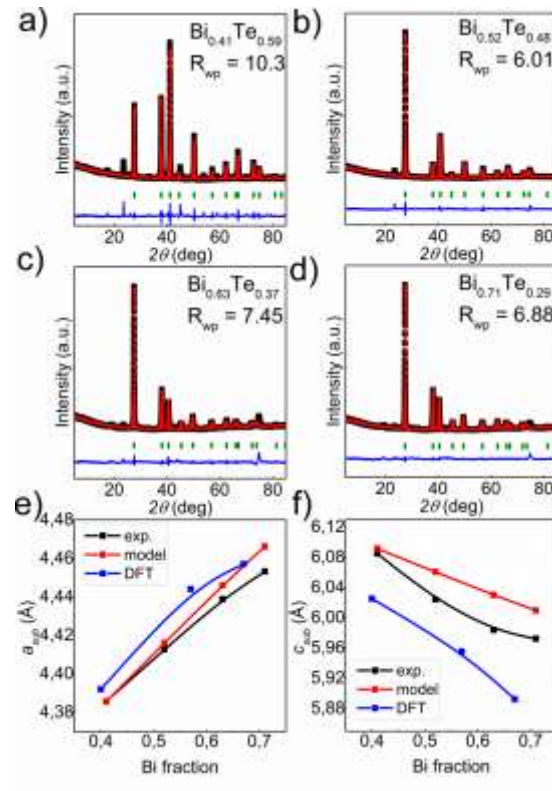


Figure 4. (a), (b), (c), (d) The results of the profile fitting with observed, calculated, and difference patterns of electrodeposited Bi_xTe_y films of different composition controlled by electrolyte composition. Dependence of the subcell parameters a_{sub} (e), and c_{sub} (f) on bismuth content in the deposited films. Red points show subcell parameters calculated for alternating Bi_2Te_3 quintuples and Bi-bilayers using stacking model[1], black points show subcell parameters determined from experimental XRD data, blue points show subcell parameters calculated using DFT.

3.4. Scanning electron microscopy (SEM) and high resolution transmission electron microscopy (HRTEM)

SEM images of the Bi_xTe_y films pulse deposited from electrolytes of different $c(\text{Bi}^{3+})/c(\text{TeO}_2)$ ratio are shown in Figure 5. The films consist of big (ca 10 μm) aggregates with high surface area. The shape of the aggregates changes from roundish at stoichiometric Bi_2Te_3 to more angular and rougher for films with high Bi content. Interestingly, small light spots appeared on SEM image (Figure 5 a), when the films were deposited with excess of Te. These spots most likely correspond to tellurium[30] which, unlike bismuth, cannot form a single phase with Bi_2Te_3 and tend to form elemental Te phase. That latter was justified by XRD of Te-rich film. No phase separation was observable in SEM images of the deposits with Bi excess.

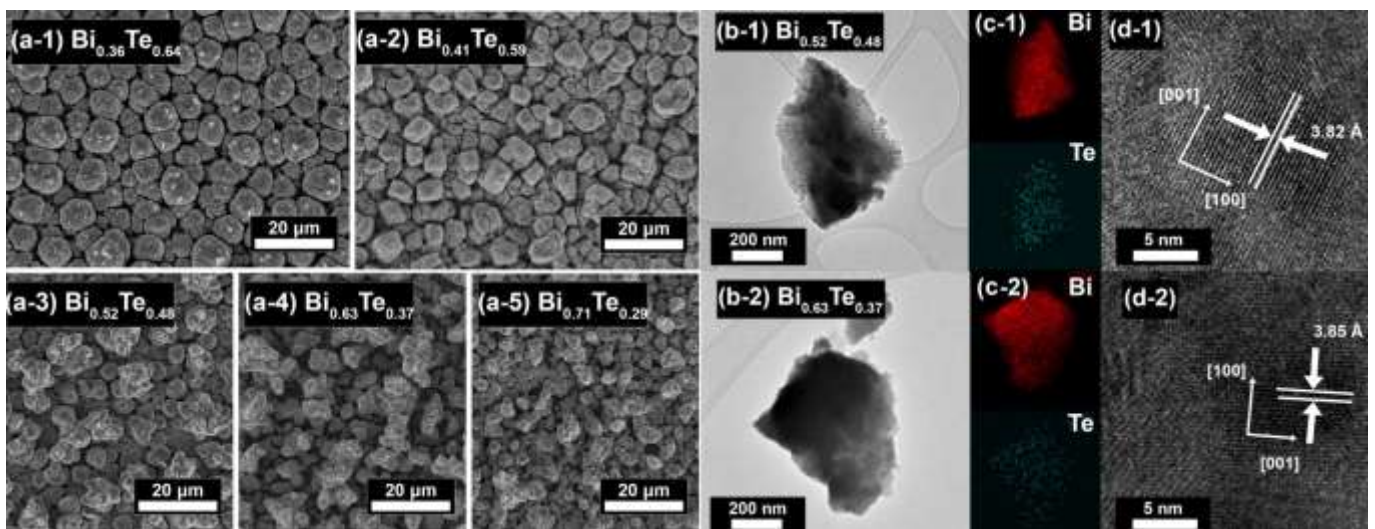


Figure 5. (a) SEM images of the electrodeposits obtained at different $c(\text{Bi}^{3+})/c(\text{TeO}_2)$ ratio. HRTEM images of Bi_xTe_y deposits: (b) overview (c) EDS elemental mapping, (d) magnified image.

Figure 5 (b-d) demonstrates HRTEM images of two Bi_xTe_y samples of different composition with elemental mapping. The mapping illustrates a uniform distribution of both elements throughout the material. Analysis of magnified parts gives values of $\{100\}$ or $\{010\}$ interplanar spacing. The change in the values of the spacing with the increase of bismuth content shown in the labels agrees with the results obtained from the profile fitting of XRD patterns shown in Figure 4.

By determining the {100} or {010} directions in the synthesized structures, we indexed the {001} direction. No periodic sequence in bright and dark spots is observed along the {001} direction in accord with aperiodic character of the superlattice, as Bi bilayers and Bi₂Te₃ quintuples alternate stochastically in accordance with the concept of the infinitely adaptive (Bi₂)_m(Bi₂Te₃)_n series.

3.5. X-ray photoelectron spectroscopy (XPS)

Bi⁰ state related to metallic bismuth was excluded by conditions of electrodeposition (sufficiently positive electrode potential applied in the anodic refinement phase of the pulsed periodic electrodeposition provided complete anodic oxidation of metallic bismuth and this was controlled by CV), therefore Bi⁰ in the pulsed electrodeposited film observable with XPS could be attributed to the interlayer bismuth, the one characterized by anodic oxidation peak **B** in Figure 2, and that was the motif for investigation of the electrodeposited films with XPS.

X-ray photoelectron spectra of (Bi₂)_m(Bi₂Te₃)_n electrodeposited films of various composition are presented in Figure 6. Analysis of the spectra has disclosed no Bi⁰ in nearly stoichiometric Bi₂Te₃ samples and the significant presence of Bi⁰ at enhanced Bi content, with the over-stoichiometric bismuth corresponding to Bi⁰ (Table 1). The similar XPS proof of Bi-bilayer formation was provided in [31–33].

Bi^{III} is represented in the spectra by Bi₂Te₃ and Bi₂O₃ joint contribution. The contribution of Bi₂O₃ did not vanish completely with argon etching, especially at the highest used Bi content, probably, due to incompact film structure which prevented from efficient elimination of the chemically adsorbed oxygen at argon etching.

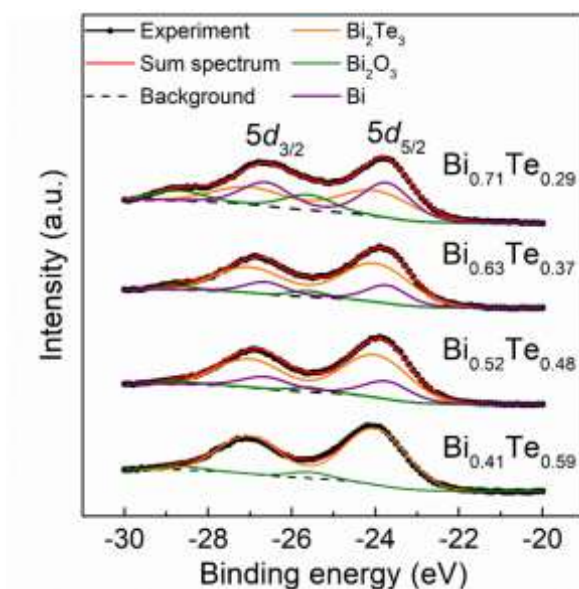


Figure 6. X-ray photoelectron spectra of $(\text{Bi}_2)_m(\text{Bi}_2\text{Te}_3)_n$ films of various stoichiometry. Dotted line represents background line, Orange - $5d_{5/2} + 5d_{3/2}$ band of Bi_2Te_3 , green - $5d_{5/2} + 5d_{3/2}$ band of Bi_2O_3 , purple - $5d_{5/2} + 5d_{3/2}$ band of Bi^0 , red line represents sum spectrum.

Table 1. Bismuth peak areas (S) in X-ray photoelectron spectra of $(\text{Bi}_2)_m(\text{Bi}_2\text{Te}_3)_n$ films of various composition and the corresponding goodness of fit. The areas are normalized for the peak area corresponding to bismuth in Bi_2Te_3 .

Composition (by atomic absorption)	$S(\text{Bi}_2\text{Te}_3)$	$S(\text{Bi}^0)$	$S(\text{Bi}_2\text{O}_3)$	χ^2
$\text{Bi}_{0.41}\text{Te}_{0.59}$	1.0	-	0.065	$1.8 \cdot 10^{-4}$
$\text{Bi}_{0.52}\text{Te}_{0.48}$	1.0	0.34	0.063	$3.9 \cdot 10^{-5}$
$\text{Bi}_{0.63}\text{Te}_{0.37}$	1.0	0.31	0.073	$2.0 \cdot 10^{-5}$
$\text{Bi}_{0.71}\text{Te}_{0.29}$	1.0	1.0	0.40	$2.2 \cdot 10^{-5}$

3.6. Selective anodic oxidation of interlayer bismuth in $(\text{Bi}_2)_m(\text{Bi}_2\text{Te}_3)_n$

Based on obtained evidences from XRD and XPS analysis of $(\text{Bi}_2)_m(\text{Bi}_2\text{Te}_3)_n$ structures formation, the

peak **B** in Figure 2 was attributed to selective anodic oxidation of Bi bilayers in the superlattice. The further logical question is: what happens with $(\text{Bi}_2)_m(\text{Bi}_2\text{Te}_3)_n$ when the superlattice structure is kept at the potential of Bi interlayer anodic oxidation? Can the interlayer bismuth leave the superlattice structure, or it remains in the oxidized state inside the structure?

Figure 7 shows stripping voltammograms of the superlattices deposited with different number of the potential controlled pulses and different deposition, E_{dep} , potentials. Potentials of the anodic refinement in the pulse deposition were set as described in Section 3.2. As the completion of the anodic oxidation of bismuth bilayer in the massive superlattice requires some time, slower scan rate in this case compared to Figure 2 was used, in order to obtain well-resolved anodic oxidation peaks.

The stripping of the deposit obtained at $E_{\text{dep}} = -0.05 \text{ V}$ discloses a single peak **C** of bismuth telluride anodic oxidation (Figure 7 a) The interlayer bismuth inclusion requires the use of lower E_{dep} (Figure 7 b,c,d).

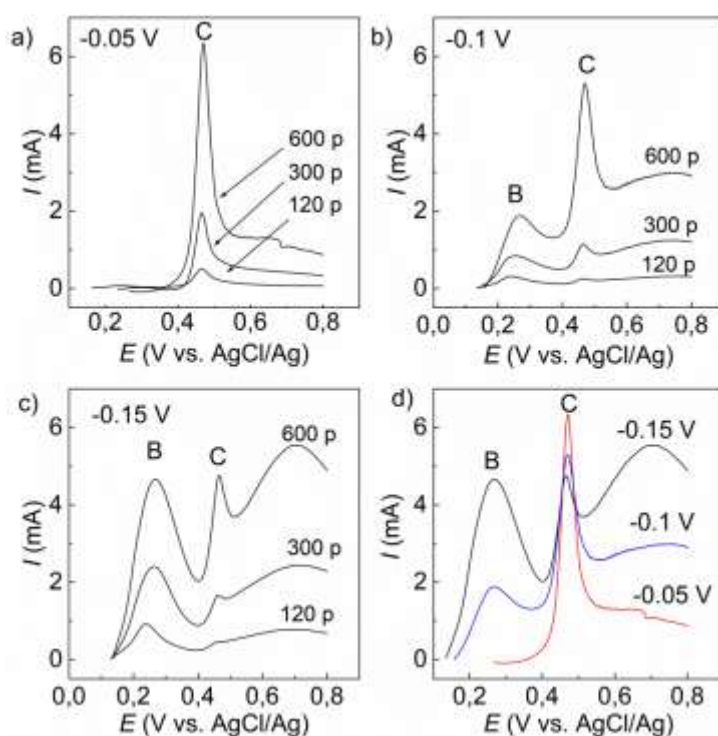
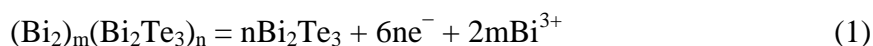


Figure 7. Stripping voltammograms of various Bi_xTe_y electrodeposits obtained by pulse deposition at $20 \text{ mmol}\cdot\text{L}^{-1} \text{ Bi}(\text{NO}_3)_3$, $10 \text{ mmol}\cdot\text{L}^{-1} \text{ TeO}_2$, $3 \text{ mol}\cdot\text{L}^{-1} \text{ HNO}_3$ with different number of pulses indicated in labels at variable E_{dep} (a) -0.05 V , (b) -0.1 V , (c) -0.15 V ; (d) 600 pulses at different E_{dep} . Electrolyte: 3

$\text{mol}\cdot\text{L}^{-1}$ HNO_3 , scan rate 5 mV s^{-1} .

For further justification of the bismuth interlayer anodic oxidation peak **B**, films of different composition using various deposition potentials and different electrolyte composition were obtained and changes in subcell parameters and elemental composition were examined upon the potentiostatic treatment at 0.38 V in $3 \text{ mol}\cdot\text{L}^{-1}$ HNO_3 for 10 minutes (Figure 8). The 0.38 V potential corresponds to the end of interlayer bismuth oxidation, but is insufficient for anodic oxidation of bismuth telluride. The results presented in Figure 8 and Table 2 show that the selective anodic oxidation at 0.38 V causes a decrease in Bi/Te ratio almost to that of stoichiometric Bi_2Te_3 which corresponds to Eq (1):



Thus, the peak **B** in stripping voltammograms is the convenient indicator of the interlayer bismuth in the electrodeposits, and this interlayer bismuth can be surprisingly easily removed by the anodic treatment. The even more surprising result is the prevention of the expanded structure in the oxidized superlattice of moderate initial bismuth content (Figure 8 *g, h*). It appears that the greater part of interlayer bismuth was transformed into cations and evacuated from the crystals in the strongly acidic medium which was used in the experiments with selective anodic oxidation of the interlayer bismuth.

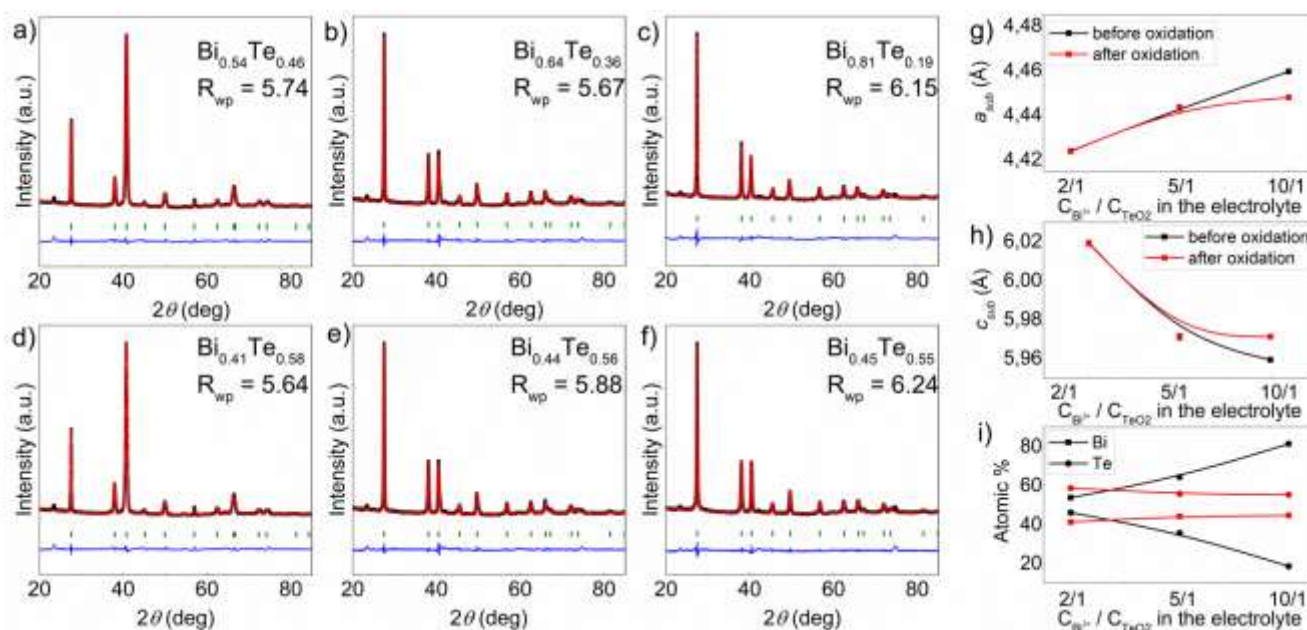


Figure 8. The results of profile fitting with observed, calculated, and difference patterns of

$(\text{Bi}_2)_m(\text{Bi}_2\text{Te}_3)_n$ films deposited from different electrolytes: $c(\text{Bi}^{3+})/c(\text{TeO}_2) = 2$ before oxidation (a); after oxidation (b); $c(\text{Bi}^{3+})/c(\text{TeO}_2) = 5$ before oxidation (c); after oxidation (d); $c(\text{Bi}^{3+})/c(\text{TeO}_2) = 10$ before oxidation (e); after oxidation (f). Dependence of a_{sub} , c_{sub} and films composition (g, h and i respectively) before (black lines) and after (red lines) oxidation of bismuth bilayers.

Table 2. EDX composition and subcell parameters obtained from profile fitting of XRD patterns of powder diffraction data of $(\text{Bi}_2)_m(\text{Bi}_2\text{Te}_3)_n$ films deposited from the electrolytes of different composition.

$\text{Bi}^{3+}/\text{TeO}_2$ in electrolyte	Before oxidation of Bi bilayers					After oxidation of Bi bilayers				
	EDX composition		a_{sub} , Å	c_{sub} , Å	R_{wp}	EDX composition		a_{sub} , Å	c_{sub} , Å	R_{wp}
	Bi, %	Te, %				Bi, %	Te, %			
2/1	53.83	46.17	4.42	6.02	5.74	41.27	58.73	4.42	6.02	5.64
5/1	64.31	35.69	4.44	5.97	5.67	44.22	55.78	4.44	5.97	5.88
10/1	81.40	18.60	4.46	5.96	6.15	44.67	55.33	4.45	5.97	5.24

This oxidative lability of the superlattice may provide novel possibility to control structure and composition of Bi_xTe_y materials that may be of interest for complex thermoelectric materials design based on bismuth telluride.

Conclusions

Superlattice structures of $(\text{Bi}_2)_m(\text{Bi}_2\text{Te}_3)_n$ series with Bi mole fraction varying from 0.41 to 0.71 were synthesized by pulse potentiostatic electrodeposition with controlled potentials of cathodic and anodic phases: the lower potential was set in the region of bismuth telluride cathodic deposition, while the upper potential was set in the region of metallic bismuth anodic oxidation, where bismuth adatoms on bismuth telluride were yet stable. The molar fraction of bismuth in the superlattices was controlled by atomic ratio

of Bi(III) and Te(IV) in the electrolyte solution.

The pulse potential control mode favored formation of compact film by providing improved mass transport of precursors. The presence of Bi⁰ valence state of the interlayer bismuth was proved. The interlayer Bi⁰ component of (Bi₂)_m(Bi₂Te₃)_n superlattices was distinguished from metallic bismuth by significantly higher potential of anodic oxidation.

An increase in the subcell parameter a_{sub} from 4.39 Å to 4.45 Å and a decrease in parameter c_{sub} from 6.09 Å to 5.97 Å with bismuth molar fraction increase from 0.41 to 0.71 was determined. The variation of the structure was confirmed by DFT calculations and high resolution transmission electron microscopy observation of the superlattices.

The potential range of the interlayer bismuth anodic oxidation is significantly below the range of bismuth telluride anodic oxidation. The separation of the two anodic reactions on the potential scale has provided the selective anodic oxidation and removal of the interlayer bismuth from the superlattice with formation of the product, which was very close to Bi₂Te₃ by stoichiometry, but differed from bismuth telluride by expanded crystal structure.

Due to advantages inherent in the electrodeposition technique (low temperature of solid phase formation, precise control of the film composition and thickness, economy and appropriateness for deposition on surfaces of complex topology), the new electrochemical method of (Bi₂)_m(Bi₂Te₃)_n superlattice structure preparation is expected to give a stimulus in the development of thermoelectric materials with controllable electrophysical properties. The discovered effect of the expanded structure preservation during the anodic oxidation and removal of the interlayer bismuth can be also of interest for other energy conversion and storage devices development based on intercalation of metal cations.

Acknowledgement

This research has received funding from Horizon 2020 research and innovation program under MSCA-RISE-2017 (No. 778357).

REFERENCES

- [1] J.W.G. Bos, H.W. Zandbergen, M.H. Lee, N.P. Ong, R.J. Cava, Structures and thermoelectric properties of the infinitely adaptive series $(\text{Bi}_2)_m(\text{Bi}_2\text{Te}_3)_n$, *Phys. Rev. B - Condens. Matter Mater. Phys.* 75 (2007) 1–9. doi:10.1103/PhysRevB.75.195203.
- [2] M. Eschbach, M. Lanius, C. Niu, E. Młyńczak, P. Gospodarič, J. Kellner, P. Schüffelgen, M. Gehlmann, S. Döring, E. Neumann, M. Luysberg, G. Mussler, L. Plucinski, M. Morgenstern, D. Grützmacher, G. Bihlmayer, S. Blügel, C.M. Schneider, Bi_1Te_1 : a dual topological insulator, *Nat. Commun.* (2017) 1–9. doi:10.1038/ncomms14976.
- [3] H. Fang, T. Feng, H. Yang, X. Ruan, Y. Wu, Synthesis and thermoelectric properties of compositional-modulated lead telluride-bismuth telluride nanowire heterostructures, *Nano Lett.* 13 (2013) 2058–2063. doi:10.1021/nl400319u.
- [4] G.J. Snyder, E.S. Toberer, Complex thermoelectric materials, *Nat. Mater.* 7 (2008) 105–114. doi:10.1038/nmat2090.
- [5] P.A. Sharma, A.L.L. Sharma, D.L. Medlin, A.M. Morales, N. Yang, M. Barney, J. He, F. Drymiotis, J. Turner, T.M. Tritt, Low phonon thermal conductivity of layered $(\text{Bi}_2)_m(\text{Bi}_2\text{Te}_3)_n$ thermoelectric alloys, *Phys. Rev. B - Condens. Matter Mater. Phys.* 83 (2011) 1–10. doi:10.1103/PhysRevB.83.235209.
- [6] J.W.G. Bos, F. Faucheux, R.A. Downie, A. Marcinkova, Phase stability, structures and properties of the $(\text{Bi}_2)_m(\text{Bi}_2\text{Te}_3)_n$ natural superlattices, *J. Solid State Chem.* 193 (2012) 13–18. doi:10.1016/j.jssc.2012.03.034.
- [7] J.R. Jeffries, A.L. Lima Sharma, P.A. Sharma, C.D. Spataru, S.K. McCall, J.D. Sugar, S.T. Weir, Y.K. Vohra, Distinct superconducting states in the pressure-induced metallic structures of the nominal semimetal Bi_4Te_3 , *Phys. Rev. B - Condens. Matter Mater. Phys.* 84 (2011) 6–9. doi:10.1103/PhysRevB.84.092505.

- [8] Y. Saito, P. Fons, K. Makino, K. V. Mitrofanov, F. Uesugi, M. Takeguchi, A. V. Kolobov, J. Tominaga, Compositional tuning in sputter-grown highly-oriented Bi-Te films and their optical and electronic structures, *Nanoscale*. 9 (2017) 15115–15121. doi:10.1039/c7nr04709f.
- [9] R. Rostek, N. Stein, C. Boulanger, A review of electroplating for V-VI thermoelectric films: From synthesis to device integration, *J. Mater. Res.* 30 (2015) 2518–2543. doi:10.1557/jmr.2015.203.
- [10] C. Boulanger, Thermoelectric Material Electroplating: a Historical Review, *J. Electron. Mater.* 39 (2010) 1818–1827. doi:10.1007/s11664-010-1079-6.
- [11] C. Lei, K.S. Ryder, E. Koukharenko, M. Burton, I.S. Nandhakumar, Electrochemical deposition of bismuth telluride thick layers onto nickel, *Electrochem. Commun.* 66 (2016) 1–4. doi:10.1016/J.ELECOM.2016.02.005.
- [12] S. Diliberto, V. Richoux, N. Stein, C. Boulanger, Influence of pulsed electrodeposition on stoichiometry and thermoelectric properties of bismuth telluride films, *Phys. Status Solidi Appl. Mater. Sci.* 205 (2008) 2340–2344. doi:10.1002/pssa.200779416.
- [13] S. Michel, S. Diliberto, C. Boulanger, N. Stein, J.M. Lecuire, Galvanostatic and potentiostatic deposition of bismuth telluride films from nitric acid solution: Effect of chemical and electrochemical parameters, *J. Cryst. Growth.* 277 (2005) 274–283. doi:10.1016/j.jcrysgro.2004.12.164.
- [14] V. Richoux, S. Diliberto, C. Boulanger, J.M. Lecuire, Pulsed electrodeposition of bismuth telluride films: Influence of pulse parameters over nucleation and morphology, *Electrochim. Acta.* 52 (2007) 3053–3060. doi:10.1016/J.ELECTACTA.2006.09.042.
- [15] A. Zhou, Q. Fu, W. Zhang, B. Yang, J. Li, P. Ziolkowski, E. Mueller, D. Xu, Enhancing the Thermoelectric Properties of the Electroplated Bi₂Te₃ Films by Tuning the Pulse Off-to-on Ratio, *Electrochim. Acta.* 178 (2015) 217–224. doi:10.1016/j.electacta.2015.07.164.
- [16] C. Schumacher, K.G. Reinsberg, R. Rostek, L. Akinsinde, S. Baessler, S. Zastrow, G. Rampelberg,

- P. Woias, C. Detavernier, J.A.C. Broekaert, J. Bachmann, K. Nielsch, Optimizations of pulsed plated p and n-type Bi₂Te₃-based ternary compounds by annealing in different ambient atmospheres, *Adv. Energy Mater.* 3 (2013) 95–104. doi:10.1002/aenm.201200417.
- [17] H. Baker, *ASM Handbook: Alloy Phase Diagrams Volume 3*, ASM International, Ohio, United States, 1998.
- [18] J.S. Anderson, On infinitely adaptive structures, *J. Chem. Soc. Dalt. Trans.* (1973) 1107–1115.
- [19] H. Lind, S. Lidin, A general structure model for Bi-Se phases using a superspace formalism, *Solid State Sci.* 5 (2003) 47–57. doi:10.1016/S1293-2558(02)00080-8.
- [20] V. Petříček, M. Dušek, L. Palatinus, Crystallographic computing system JANA2006: General features, *Zeitschrift Fur Krist.* 229 (2014) 345–352. doi:10.1515/zkri-2014-1737.
- [21] and C.J.P. Alexander V. Naumkin, Anna Kraut-Vass, Stephen W. Gaarenstroom, NIST X-ray Photoelectron Spectroscopy Database, (n.d.). doi:10.18434/T4T88K.
- [22] G. Kresse, J. Furthmüller, Efficient iterative schemes for ab initio total-energy calculations using a plane-wave basis set, *Phys. Rev. B - Condens. Matter Mater. Phys.* 54 (1996) 11169–11186. doi:10.1103/PhysRevB.54.11169.
- [23] J.P. Perdew, K. Burke, M. Ernzerhof, The stability of ionic crystal surfaces. *Journal of Physics C: Solid State Physics*, 12(22), 4977., *Phys. Rev. Lett.* 77 (1996) 3865–3868. doi:10.1103/PhysRevLett.77.3865.
- [24] S. Grimme, J. Antony, S. Ehrlich, H. Krieg, A consistent and accurate ab initio parametrization of density functional dispersion correction (DFT-D) for the 94 elements H-Pu, *J. Chem. Phys.* 132 (2010). doi:10.1063/1.3382344.
- [25] Y. Ma, A. Johansson, E. Ahlberg, A.E.C. Palmqvist, A mechanistic study of electrodeposition of bismuth telluride on stainless steel substrates, *Electrochim. Acta.* 55 (2010) 4610–4617. doi:10.1016/J.ELECTACTA.2010.03.018.

- [26] P. Magri, C. Boulanger, J.-M. Lecuire, Synthesis, properties and performances of electrodeposited bismuth telluride films, *J. Mater. Chem.* 6 (1996) 773–779. doi:10.1039/jm9960600773.
- [27] E.J. Menke, Q. Li, R.M. Penner, Bismuth telluride (Bi_2Te_3) nanowires synthesized by cyclic electrodeposition/stripping coupled with step edge decoration, *Nano Lett.* 4 (2004) 2009–2014. doi:10.1021/nl048627t.
- [28] M.S. Martín-González, A.L. Prieto, R. Gronsky, T. Sands, A.M. Stacy, Insights into the Electrodeposition of Bi_2Te_3 , *J. Electrochem. Soc.* 149 (2002) C546. doi:10.1149/1.1509459.
- [29] A.S. Bakavets, Y.M. Aniskevich, G.A. Ragoisha, E.A. Streltsov, Bismuth and lead underpotential deposition on bismuth telluride: new insights into the electrochemical synthesis of bismuth telluride and evaluation of real surface area, *J. Belarusian State Univ. Chem.* 1 (2017) 3–13.
- [30] A.S. Bakavets, Y.M. Aniskevich, G.A. Ragoisha, E.A. Streltsov, Underpotential deposition of lead onto $\text{Bi}_2\text{Te}_3/\text{Te}$ heterostructures, *Electrochem. Commun.* 94 (2018) 23–26. doi:10.1016/j.elecom.2018.07.018.
- [31] Q.D. Gibson, L.M. Schoop, A.P. Weber, H. Ji, S. Nadj-Perge, I.K. Drozdov, H. Beidenkopf, J.T. Sadowski, A. Fedorov, A. Yazdani, T. Valla, R.J. Cava, Termination-dependent topological surface states of the natural superlattice phase Bi_4Se_3 , *Phys. Rev. B - Condens. Matter Mater. Phys.* 88 (2013) 1–5. doi:10.1103/PhysRevB.88.081108.
- [32] T. Valla, H. Ji, L.M. Schoop, A.P. Weber, Z.H. Pan, J.T. Sadowski, E. Vescovo, A. V. Fedorov, A.N. Caruso, Q.D. Gibson, L. Müchler, C. Felser, R.J. Cava, Topological semimetal in a Bi- Bi_2Se_3 infinitely adaptive superlattice phase, *Phys. Rev. B - Condens. Matter Mater. Phys.* 86 (2012) 3–7. doi:10.1103/PhysRevB.86.241101.
- [33] I.I. Klimovskikh, D. Sostina, A. Petukhov, A.G. Rybkin, S. V. Eremeev, E. V. Chulkov, O.E. Tereshchenko, K.A. Kokh, A.M. Shikin, Spin-resolved band structure of heterojunction Bi-bilayer/3D topological insulator in the quantum dimension regime in annealed $\text{Bi}_2\text{Te}_{2.4}\text{Se}_{0.6}$, *Sci. Rep.* 7 (2017) 2–7. doi:10.1038/srep45797.